

# Non-destructive evaluation and pattern recognition for SCRC columns using the AE technique

Fangzhu Du and Dongsheng Li\*

*School of Civil Engineering, Dalian University of Technology, China*

*(Received March 6, 2019, Revised April 29, 2019, Accepted August 27, 2019)*

**Abstract.** Steel-confined reinforced concrete (SCRC) columns feature highly complex and invisible mechanisms that make damage evaluation and pattern recognition difficult. In the present article, the prevailing acoustic emission (AE) technique was applied to monitor and evaluate the damage process of steel-confined RC columns in a quasi-static test. AE energy-based indicators, such as index of damage and relax ratio, were proposed to trace the damage progress and quantitatively evaluate the damage state. The fuzzy C-means algorithm successfully discriminated the AE data of different patterns, validity analysis guaranteed cluster accuracy, and principal component analysis simplified the datasets. A detailed statistical investigation on typical AE features was conducted to relate the clustered AE signals to micro mechanisms and the observed damage patterns, and differences between steel-confined and unconfined RC columns were compared and illustrated.

**Keywords:** steel-confined RC structure; acoustic emission; damage evaluation; cluster analysis; pattern recognition

## 1. Introduction

Steel-confined reinforced concrete (RC) columns are widely used in civil engineering, especially in high-rise buildings, large-span bridges, and massive structures. The casing steel tube serves as a formwork and protective jacket that constrains the plastic deformation of core concrete and prevents premature shear failure (Han *et al.* 2009). Several scholars (Liu *et al.* 2009, Wang *et al.* 2017, Zhou *et al.* 2008) have investigated the mechanical behavior of steel-confined RC columns under different loading conditions and proved that the proposed column features good confinement effects, loading capacity, and anti-seismic capacity. The wide utilization of steel-confined RC column emphasizes the necessity of developing structural health monitoring (SHM) and evaluating approaches.

Acoustic emission (AE) is a non-destructive technique that can provide reliable and real-time information on various structures; it has been widely explored in civil engineering for SHM and damage recognition (Abouhussien and Hassan 2017). At present, most studies on AE utilization are focused on concrete structures (Behnia *et al.* 2014, Carpinteri *et al.* 2011) and steel materials (Droubi *et al.* 2017). Due to the highly complex and invisible damage patterns, few studies have

---

\*Corresponding author, Professor, E-mail: lidongsheng@dlut.edu.cn

paid attention to AE detection for composite structures. Behnia *et al.* (2016) applied the AE technique to detect the fracture process of steel fiber-reinforced concrete beams subjected to pure torsion. Ma *et al.* (2017) reported an AE-based damage assessment method for FRP-strengthened RC columns during a pseudo static test. Li *et al.* (2017) and Du *et al.* (2018) thoroughly investigated the AE behavior of steel-confined RC columns and FRP-confined concrete-filled steel tubular columns under different loading conditions and proposed indicators to evaluate the damage state, describe the damage mechanisms, and provide critical warning. However, quantitative evaluations of damage severity have not been investigated comprehensively, and the damage classification and failure pattern of steel-confined RC columns have not been addressed.

Compared with traditional RC columns, steel-confined RC columns offer a highly complex and invisible failure mechanism by combining steel tube, anisotropic concrete, and steel rebar; such a structure however, makes the damage recognition very cumbersome. Damages caused by concrete cracking (micro and macro), steel/concrete interface slipping and friction, steel deformation (elastic and plastic), and ambient noises are inevitable during the damage process of steel-confined RC columns. Thus, correct identification of these damage modes can help us illustrate the related damage mechanisms, determine major damages and take niche-targeting rehabilitation measures.

Previous research shows that cluster analysis can be successfully used for damage pattern classification and recognition for different materials. Among numerous cluster algorithms, the unsupervised k-means cluster and fuzzy C-means (FCM) cluster are used most often. For example, Pashmforoush *et al.* (2012) characterized the damage pattern of glass/epoxy composite specimens during three-point bending tests using the k-means and genetic algorithms. Griffin *et al.* (2014) conducted fuzzy C-clustering to discriminate three different AE signals during the grinding process of alloys. Marec *et al.* (2008) applied principal component analysis (PCA) to reduce data redundancy and the FCM approach to cluster the principal components into different types. To date, cluster analysis is mainly applied in damage recognition for composite or metal materials; applications of cluster analysis for steel-concrete composite structures have not been reported.

In the current study, the AE technique is applied to trace and recognize the damage evolution of steel-confined RC columns during a quasi-static test. The contributions of this study are threefold. First, energy-based indicators such as index of damage (ID) and relax ratio, are proposed to trace the damage evolution and quantitatively evaluate the damage state and typical damage stages. Second, PCA and cluster validity analysis are conducted to ensure clustering accuracy and simplify the clustering process. Finally, identification of different damage patterns is achieved on the basis of FCM cluster and statistical analysis of typical AE features.

## 2 Data processing algorithms

### 2.1 Acoustic emission energy-based indicators

The AE phenomenon is simulated by the sudden release of stored energy during material degradation and contains useful information on the damage initiation, internal condition, and failure pattern for different materials. AE features, such as amplitude, energy, duration, rise time, counts, intensity, and frequency, are commonly extracted to analyze the micro damage mechanisms of different structures. Sagar *et al.* (2015) provided a thorough description of AE features.

From the perspective of energy, material damage can be considered an energy-driven instability process. Thus, AE energy is a prevailing indicator of damage evaluation. Benavent–Climent *et al.* (2012) used the energy-based ID to correlate the AE and plastic strain energies of concrete slabs under seismic loading. ID is defined as the cumulative energy recorded at any moment during the loading cycle ( $E_{AE}$ ) divided by the cumulative energy when the structure experiences the maximum allowable damage ( $E_{AE}^D$ )

$$ID = \frac{E_{AE}}{E_{AE}^D} \quad (1)$$

Colombo *et al.* (2005a, b) proposed the relax ratio to determine the residual strength of concrete structures. This method is based on the theory that the normal release of AE energy during the unloading phase of AE testing is a sign of severe damage. The relax ratio (Eq. (2)) can be computed as the ratio of the average energy during unloading (AEU) to the average energy during loading (AEL), which explains the link between AE energy and failure loads.

$$Relax\ Ratio\ (RR) = AEU / AEL. \quad (2)$$

where the *AEL* can be defined as the cumulative energy released during loading divided by the total AE hits recorded during loading, and the *AEU* can be defined as the cumulative energy released during unloading divided by the total AE hits recorded during unloading.

### 2.2 Principal component analysis

PCA has been demonstrated to be a useful tool for dimension reduction and signal classification. PCA projects *n*-dimensional data matrix into *k* dimensional space ( $k < n$ ). The procedure of PCA can be expressed as a splitting of original data into a sum of matrix products,  $TP^T$ , and a residual matrix *E* (Manson *et al.* 2001) (Eq. (3))

$$X = TP^T + E, \quad (3)$$

where *T* is the score matrix corresponding to the principal components, *P* is the weight matrix containing each variable's weight vector, and *E* is the residual matrix representing the part of the original data that has not been considered in  $TP^T$ . Fig. 1 shows two principal components (PC1 and PC2).

In general, sample normalization is conducted to guarantee that all data matrices are comparable with one another before PCA. In this study, the maximum–minimum value method is introduced to normalize the selected AE data of different magnitudes into a specified range (0 to 1).

### 2.3 Cluster validity analysis

Several indicators, such as the Xie–Beni index (*XB*), Davies–Bouldian index (*DB*), Dunn index, partition coefficient, and classification entropy, can be used for cluster validity analysis. In this study, the *DB* and *XB* indexes were calculated to determine the optimal cluster number.

1) *DB* (Davies and Bouldin 1979). The *DB* index checks the dissimilarity of intra and inter cluster based on the inherent data set. Equation 4 provides the mathematical formulation of *DB* index

$$DB = \frac{1}{n} \sum_{i=1}^n \max_{i \neq j} \left( \frac{\sigma_i + \sigma_j}{d(c_i, c_j)} \right) \quad (4)$$

where  $n$  is the cluster number,  $\sigma_i$  represents the average distance of all nodes to its cluster center  $c_i$  (intra distance), and  $d(c_i, c_j)$  denotes the centroid distance of two different clusters (inter distance). A small  $DB$  index yields good clustering results.

2)  $XB$  (Xie and Beni 1991). The  $XB$  index is based on the fuzzy clustering method and defined as follows

$$XB(U, V, c) = \frac{\frac{1}{n} \sum_{i=1}^c \sum_{j=1}^n u_{ij}^m \|v_i - x_j\|^2}{\min \|v_i - v_j\|^2} \quad (i \neq j) \quad (5)$$

where  $c$  is the cluster number,  $n$  is the object number,  $u_{ij}$  represents the membership value of the  $j$ th object belonging to the  $i$ th category,  $x_j$  represents the  $j$ th object in the  $i$ th category, and  $v_i$  is the  $i$ th cluster center. A local minimum  $XB$  value indicates good cluster validity.

#### 2.4 Fuzzy C-means algorithm

Different from the hard cluster algorithms, such as k-means, which classifies a data point as either belonging to a cluster or not, the FCM algorithm permits each data point to belong to a cluster specified by a membership grade to some degree (varying within  $[0, 1]$ ). This algorithm aims to find the cluster centers  $C_i$  to minimize the feature function  $J$  by iteration (Marec *et al.* 2008).

$$J(U, V) = \sum_{j=1}^n \sum_{i=1}^k [u_i(x_j)]^f d^2(x_j, C_i) \quad (6)$$

where  $k$  is the cluster number,  $f$  is the fuzzy degree,  $U$  denotes the fuzzy membership grade matrix with  $k$  lines and  $n$  columns, and  $V$  represents the matrix for cluster centers  $C_i$ . For example

$$U = \begin{bmatrix} u_1(x_1) & u_1(x_2) & \dots & u_1(x_n) \\ u_2(x_1) & u_2(x_2) & \dots & u_2(x_n) \\ \dots & \dots & \dots & \dots \\ u_k(x_1) & u_k(x_2) & \dots & u_k(x_n) \end{bmatrix} \quad (7)$$

$$V = [C_1 | C_2 | \dots | C_m] \quad (8)$$

where  $u_i(x_j)$  is the membership value of  $j$ th data point to the  $i$ th cluster under the condition

$$\sum_{i=1}^k u_i(x_j) = 1 \quad \forall j \quad (9)$$

where  $d(x_j, C_i)$  denotes the similarity matrix between the data point  $x_j$  and its cluster center

calculated from Eq. (10).

$$d(x_j, C_i) = \sqrt{(x_j - C_i)^T (x_j - C_i)} \tag{10}$$

More algorithm details can be found in Sahu’s paper (Sahu *et al.* 2012). The flow chart of the FCM algorithm is explained in Fig. 2.

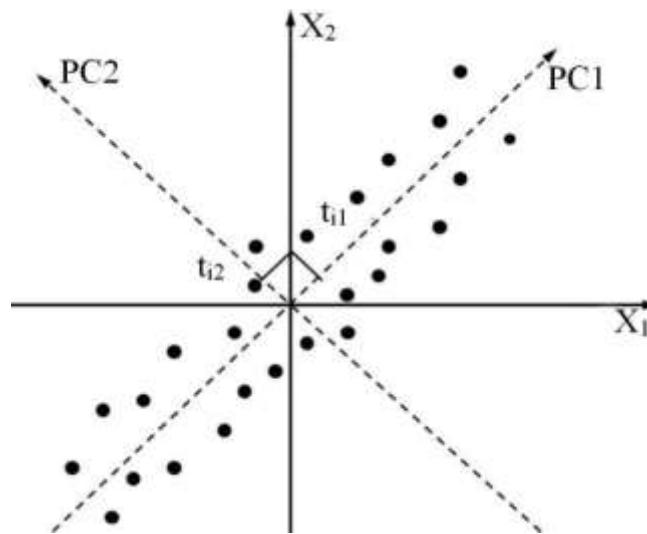


Fig. 1 Description of components analysis

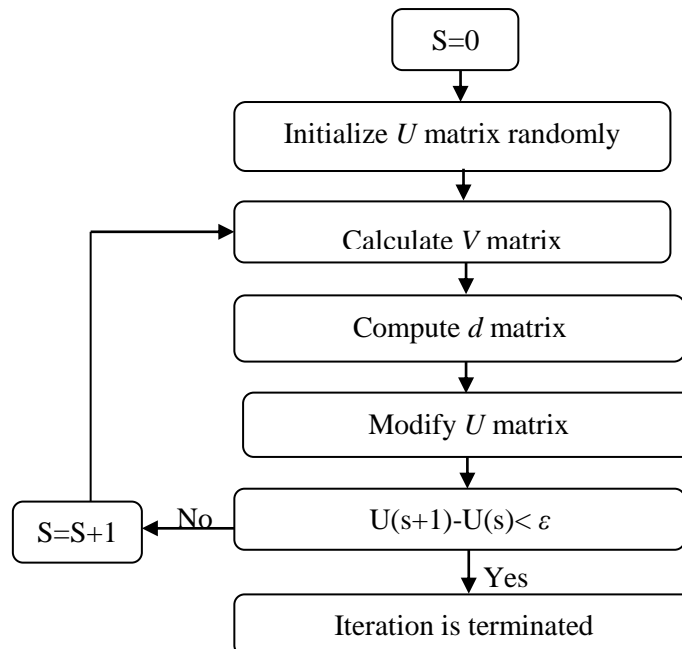


Fig. 2 Flow chart of FCM algorithm

### 3. Description of the experiment

A total of six columns were fabricated with a cross section of 300 mm × 300 mm, and three of which were confined by steel tubes. Each test specimen has a total height of 1950 mm. Fig. 3 provides the details of the specimens. The steel tube used in the experiment is Steel Q345 with a thickness of 3 mm; C40 commercial concrete, which has a measured compressive strength of 40.4 MPa, is also used. Table 1 shows the detailed properties of the test materials, and Table 2 presents the detailed design parameters for each test group; here, QSS0 and QSS3 are used to distinguish the conventional RC columns and steel-confined RC columns for conciseness, respectively.

Fig. 4 illustrates the test setup diagram, in which the prepared column–footing assemblages were subjected to combined constant axial and reciprocating lateral loads. A calibrated load cell was used to measure the axial pressure, displacement meters were applied to capture the lateral displacement, and strain gages were glued to the surface of the specimens to record their strain response. Fig. 5 presents the loading protocol for each test group. When the lateral loading decreased to approximately 70%–80% of the ultimate lateral loading, the test was terminated. More details on this test can be found in the literature (Du *et al.* 2018).

Four R-15a AE sensors with resonant frequency bands ranging from 50 kHz to 200 kHz were fixed on both sides of the columns to monitor the damage process (Fig. 4). Table 3 shows data acquisition features of the AE system. Additional details can be found in the literature (Du *et al.* 2018).

Table 1 Detail material properties

Material	Yield Strength (MPa)	Tensile Strength (MPa)	Elastic Modulus (GPa)	Thickness or Diameter (mm)	Elongation ( % )
steel tube	280	414	210	3	10.9
Rebar	420	590	205	16	17.5
Stirrup	400	525.4	206	8	18.3

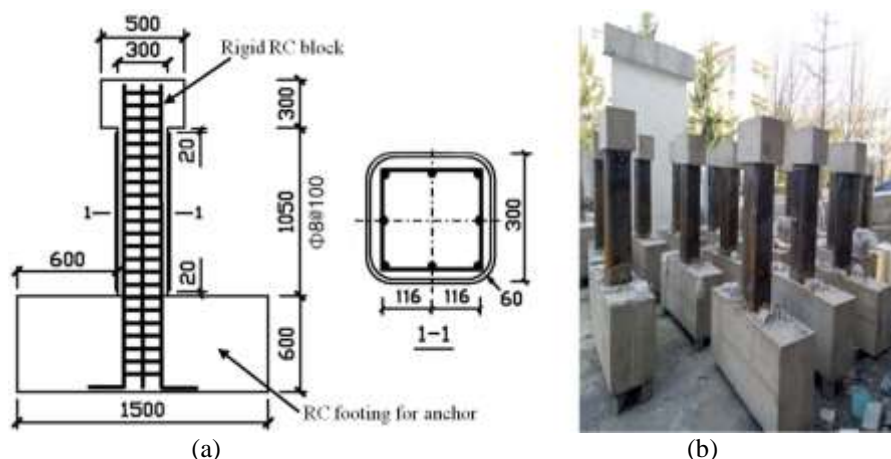


Fig. 3 Construction information of test specimens: (a) geometric details of the specimens and (b) photograph of the test specimens

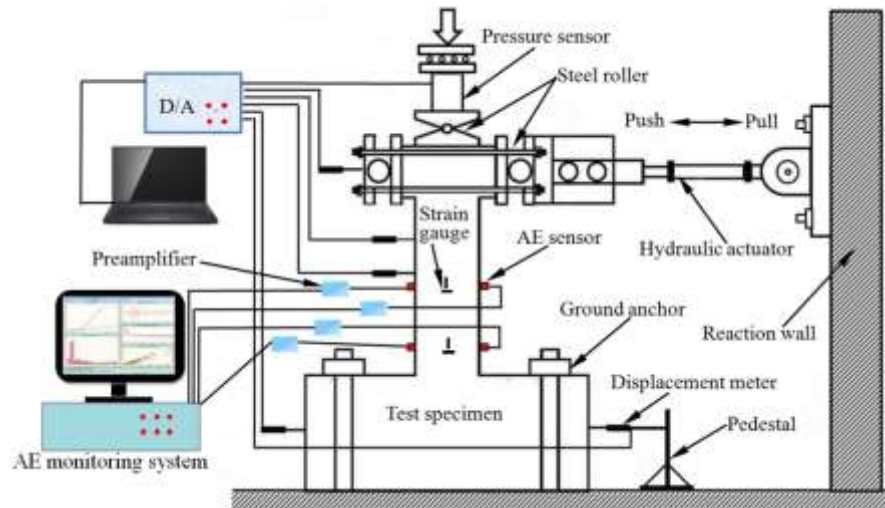


Fig. 4 Experimental facilities and data acquisition system

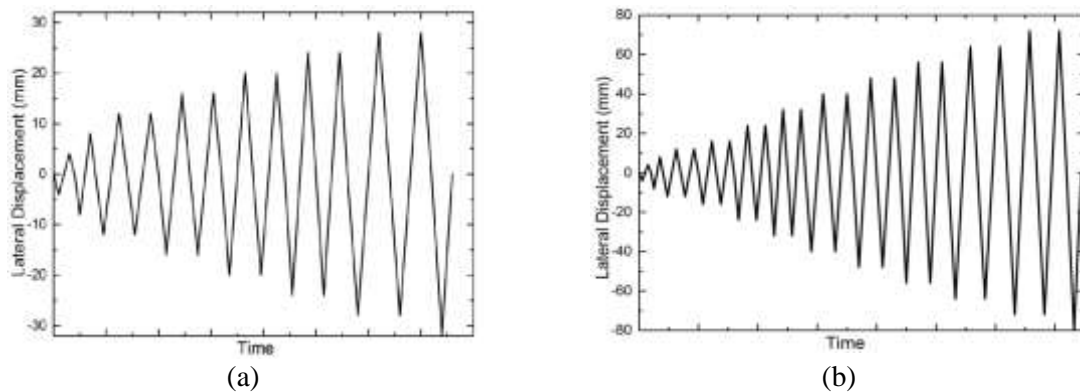


Fig. 5 Loading schemes: (a) unconfined RC columns (QSS0) and (b) steel-confined RC columns (QSS3)

Table 2 Detail information of test groups

Test Group	Specimen Number	Steel Tube	Longitudinal Rebar	Stirrups	Concrete	Axial Compression Ratio	Shear Span Ratio
QSS0	3	none	6 16	8@100	C40	0.3	4
QSS3	3	3 mm	6 16	8@100	C40	0.3	4

Table 3 Data acquisition features for the AE system

Sensor type	Peak response frequency/kHz	Threshold	Sampling rate	Sampling points	PDT/ $\mu$ s	HDT/ $\mu$ s	HLT/ $\mu$ s
R-15a	150	45 dB	1 MSPS	1024	300	800	1000

#### 4. Quantitative evaluation based on acoustic emission indicators

In a previous study, Du *et al.* (2018) reported that steel-confined RC columns show better loading capacity and favorable hysteretic responses than unconfined columns. Herein, the damage process was evaluated in three stages based on energy fluctuations, and the energy-based Sentry function successfully revealed the damage evolution and energy transition of the specimens. In this study, energy-based indicators, including ID and relax ratio, were further investigated to provide a quantitative evaluation of steel-confined RC columns.

All applied loads and released AE signals were recorded during the test. Table 4 provides the basic test results. Fig. 6 provides the typical AE signals of different damage state. As no significant difference were observed among the same test group, QSS001 and QSS301 were considered as representative specimens and are discussed in the following chapter for conciseness. Fig. 7 provides the damage patterns of specimens QSS001 and QSS301.

Table 4 Basic test results of each column-footing assemblage

Unconfined group	Load/kN	Total AE energy (mV $\cdot\mu$ s)	Total AE hits	Confined group	Load/kN	Total AE energy (mV $\cdot\mu$ s)	Total AE hits
QSS001	129.6	33469378	846028	QSS301	160.2	6312704	855610
QSS002	136.5	35726970	901561	QSS302	173.8	7011376	948138
QSS003	122.3	32687343	829574	QSS303	154.1	6772152	899737

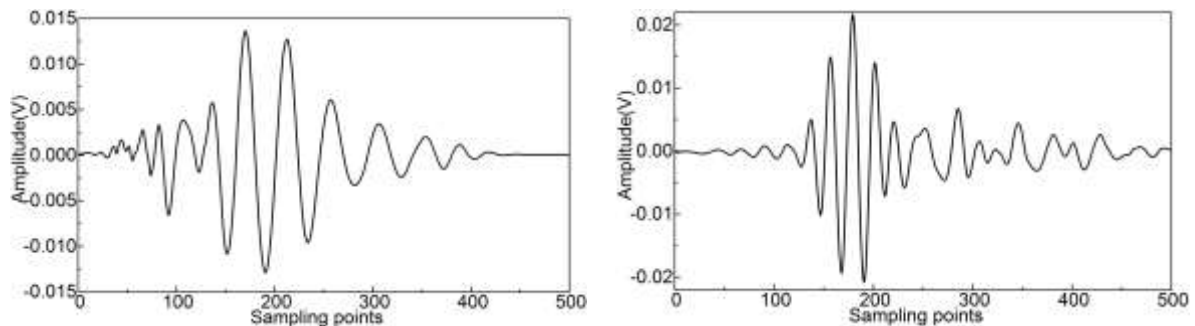


Fig. 6 Typical AE signals during the damage process



Fig. 7 Damage pattern and failure mode: (a) unconfined RC column QSS001 and (b) steel confined RC column QSS003

#### 4.1 ID analysis

Table 5 provides the calculated IDs of each loading cycle for all test specimens. ID was calculated at two points in the first two cycles and at only one point in subsequent cycles. Fig. 8 illustrates the increasing trend of ID versus loading history for specimens QSS001 and QSS301. The three evaluated stages were marked by a dashed line.

The ID of specimen QSS001 (Fig. 8(a)) linearly increased at a low rate until the maximum lateral load, indicating the stable development of concrete damage and weak concrete cracking intensity. Subsequently, the ID exponentially increased with continuous decreases in lateral loads, thereby implying that unstable development of exiting cracks causes severe damages to the test specimen. The ultimate ID value of QSS001 was 26.

Table 5 Calculated IDs for each test specimen (only first fifteen cycles for group QSS3)

Cycle ID	Cycle														
	1	2	3	4	5	6	7	8	9	10	11	12	13	14	15
QSS001	0.08	0.15	0.22	0.45	1.00	1.24	2.20	2.70	4.16	5.48	8.48	11.38	15.90	19.71	25.89
QSS002	0.09	0.17	0.25	0.48	1.00	1.32	2.37	2.95	3.86	5.21	8.14	11.03	15.47	19.30	24.97
QSS003	0.06	0.12	0.23	0.47	1.00	1.28	2.45	3.26	4.43	5.85	9.36	12.21	16.78	20.57	27.94
QSS301	0.06	0.15	0.40	0.69	1.00	1.52	1.95	2.20	3.21	3.70	4.37	4.79	5.45	5.87	6.38
QSS302	0.11	0.18	0.34	0.52	1.00	1.41	1.84	2.16	3.19	3.77	4.43	4.95	5.58	6.10	6.57
QSS303	0.07	0.22	0.47	0.65	1.00	1.63	2.11	2.64	3.36	3.89	4.58	5.02	5.51	5.95	6.30

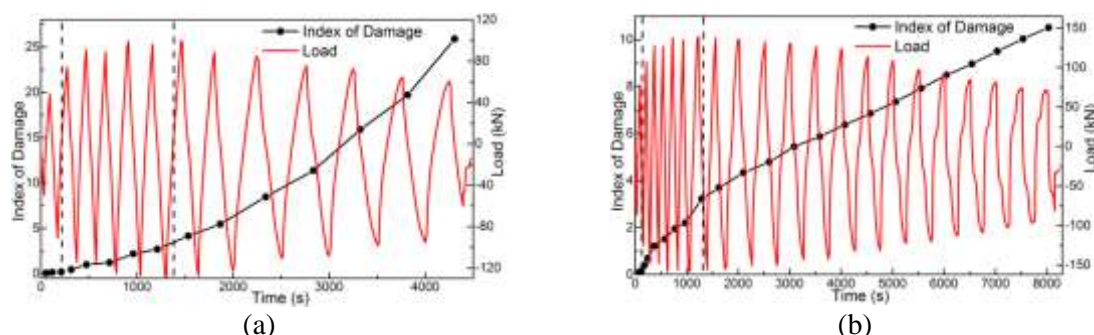


Fig. 8 History curve of load versus ID: (a) unconfined column and (b) steel-confined column

The ID of the steel-confined RC column QSS301 was significantly different from that of QSS001. During the first two stages of loading, the ID of QSS301 rapidly increased, that can be attributed to the constraining effect of the steel stub, which causes high global stiffness. Thus, a large amount of energy is required to deform the confined columns. In stage 3, the ID increased in a slow rate, which indicates progressive damage to the core concrete. The ultimate ID of QSS301 was approximately 6.4.

The ultimate ID of QSS301 (about 6.4) was only a quarter that of QSS001 (nearly 26), which means lighter damage occurred on the steel-confined columns in comparison with that on conventional columns. This result is corroborated by the damage pattern shown in Fig. 7. In addition, at the end of stage 2 (maximum load), the IDs of QSS001 and QSS301 were approximately 4.0. At this time, the test columns completely yielded. Thus, an ID of 4.0 is a good indicator of structural yielding and initial occurrence of severe damage. The increase rate of ID can also be used to depict the growth intensity of damages.

#### 4.2 Relax ratio analysis

Given its quantitative superiority, the relax ratio was calculated for each deformation level based on Eq. (2) (Table 6). Fig. 9 depicts the relationship between relax ratio and lateral load. The variations in relax ratio of all specimens showed similar results and are in accordance with the three evaluated damage stages.

In stage 1, nearly no accumulation of AE energy was observed, and the relax ratio continuously increased but maintained a low value (less than 0.4), indicating that slight concrete damages occurred. Subsequently, an increasing trend of relax ratio was observed with the slow increase of lateral load, likely because the closure and friction of existing cracks during the unloading stage also generates a large number of AE hits. The relax ratio reached approximately 1.0 at the maximum load, after which the specimens were damaged into a relax stage (stage 3). In stage 3, the accelerated mutual penetration and closure of existing cracks promoted AE activities in the unloading phase, thereby enabling the relax ratio to exceed 1.0.

A relax ratio of 0.4 may be used as an indicator of initial yielding, whereas a relax ratio of 1.0 could be a good indicator of the beginning of severe damage. When the relax ratio was less than 0.4, the columns were in a safe state, and only slight damage occurred. The increment of relax ratio from 0.4 to 1.0, corresponding to the yielding process, shows that the structure was relatively safe, although some notable damages occurred. When the relax ratio was higher than 1.0, severe damages occurred, and the columns were in an unstable stage.

Table 6 Fluctuate of Relax Ratio for each test specimen (only first sixteen cycles for group QSS3)

Cycle CSS	1	2	3	4	5	6	7	8	9	10	11	12	13	14	15	16
QSS001	0.21	0.10	0.25	0.49	0.25	0.50	0.62	0.42	0.47	1.13	1.04	0.93	1.74	1.05	1.48	0.88
QSS002	0.13	0.23	0.34	0.31	0.42	0.59	0.76	0.61	0.79	1.27	1.10	1.02	1.47	1.55	1.29	1.04
QSS003	0.17	0.35	0.28	0.42	0.35	0.44	0.57	0.73	0.53	1.05	1.27	1.51	1.18	1.40	1.58	1.21
QSS301	0.24	0.38	0.48	0.77	0.57	0.65	0.74	0.85	0.99	1.02	1.42	1.07	1.70	1.35	1.31	1.15
QSS302	0.16	0.31	0.54	0.72	0.53	0.46	0.77	0.89	1.05	1.34	1.50	1.41	1.78	1.56	1.22	1.08
QSS303	0.22	0.43	0.31	0.64	0.45	0.67	0.80	1.06	1.30	0.92	1.26	1.35	1.67	1.44	1.59	1.23

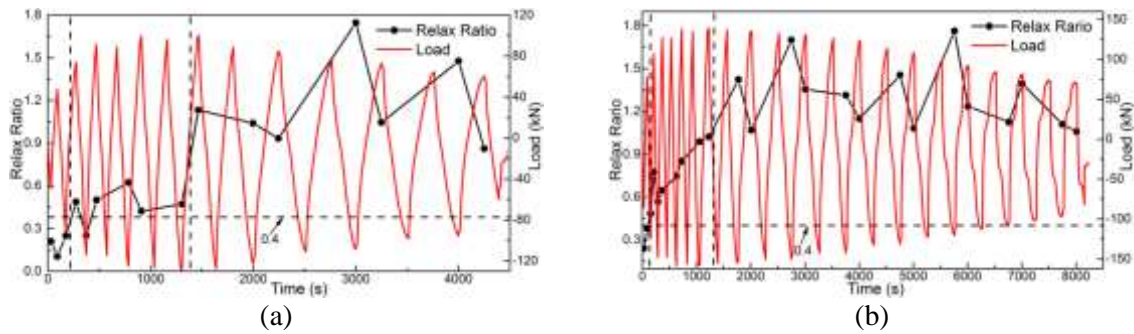


Fig. 9 History curve of load versus relax ratio: (a) unconfined column and (b) steel confined column

In comparison, the variations in ID and relax ratio provide quantitative information on damage severity. High IDs and relax ratios provide critical warnings of the potential occurrence of severe damage. In practical application, variations in ID and relax ratio can mutually support quantitative evaluations of structural damages and provide useful information for operation and management.

### 5. Damage pattern recognition by clustering analysis

Clustering analysis classifies  $n$  elements into  $k$  representative classes with different characteristics. In general, elements in the same cluster are similar; otherwise, the elements are alienated. The classified  $k$  clusters can be related to different damage types. In this section, the AE parameter-based FCM cluster method was conducted to identify different damage patterns in the test columns. The selected AE features were amplitude, counts, energy, rise time, duration, intensity, and peak frequency; these features were used as an initial set of vectors during the clustering process. PCA was conducted to project the selected AE features into low, irrelevant dimensions to eliminate redundancy. In this study, the top three principal components were used in the FCM algorithm to classify  $n$  AE signals into  $k$  classes. Cluster validity indicators ( $DB$  and  $XB$ ) were calculated to determine the optimal cluster number ( $k$ ).

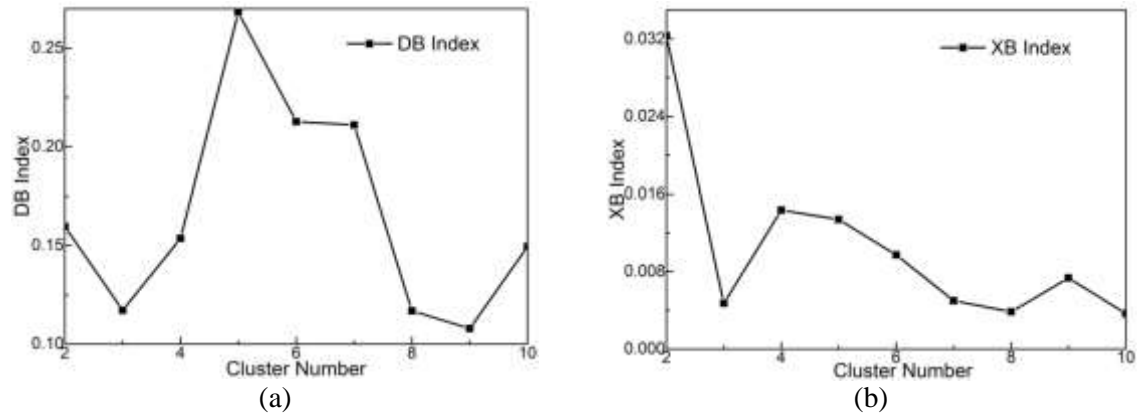


Fig. 10 Cluster validity analysis for unconfined column QSS001: (a) *DB* index and (b) *XB* index

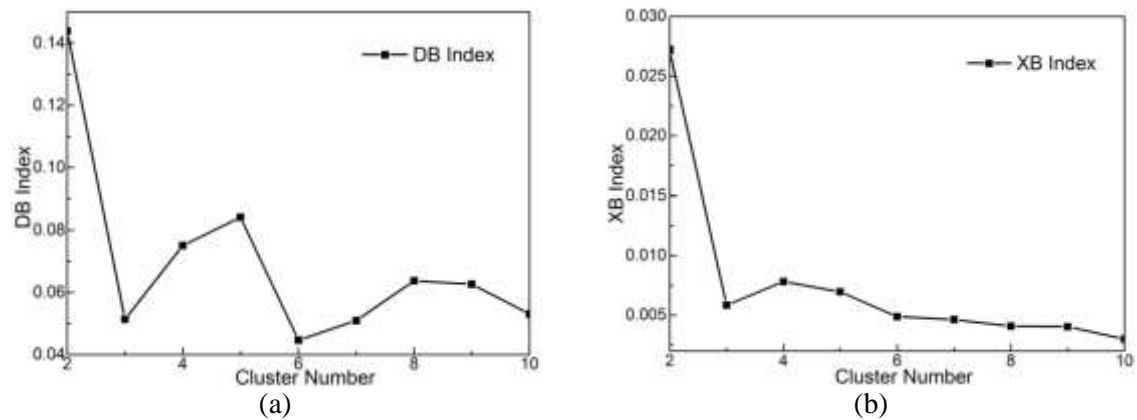


Fig. 11 Cluster validity analysis for steel confined column QSS301, (a) *DB* index and (b) *XB* index

### 5.1 Determination of the optimal cluster number

During validity analysis, the cluster number ranged from 2 to 10. Figs. 10 and 11 show the indicators (*DB* and *XB*) change with the cluster number. The *DB* index for specimen QSS001 achieved a local minimum value when the cluster numbers ( $k$ ) were 3 and 9; by comparison, the *XB* index reached a local minimum value at cluster numbers 3 and 8. For QSS301, the *DB* and *XB* indices reached local minima when the cluster number was 3. In summary, the *XB* and *DB* indices reached local minima when the cluster number was 3 for both confined and unconfined RC columns. Therefore, the optimal cluster number is 3.

### 5.2 Damage patterns corresponding to cluster outcomes

The FCM algorithm was conducted to classify the AE signals recorded during the pseudo-static loading test into three representative classes according to their inherent data structure. The fluctuation of AE features and correlativity charts of different AE features after clustering are shown in Figs.

12-15. As shown in the cluster results, the principal component (PC1 and PC2) correlogram and two-dimensional cross-plot of typical AE features distinguished the three types of damage signals accurately. The statistical value of typical AE features for the three clusters are shown in Tables 7 and 8.

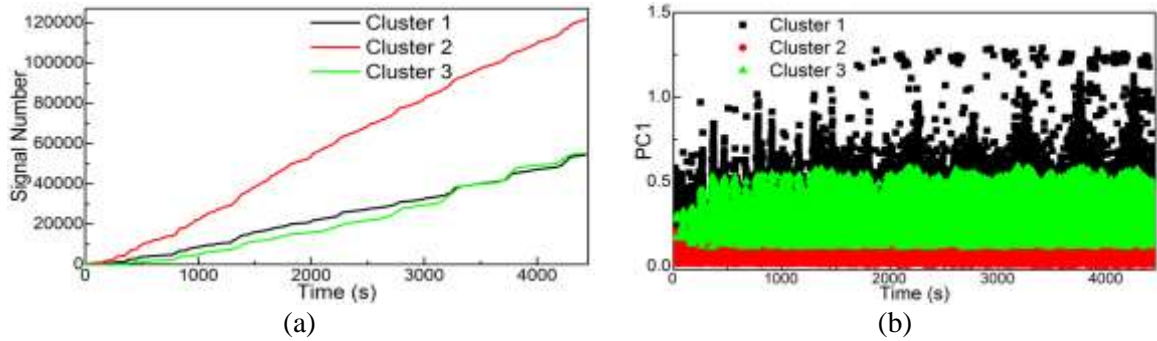


Fig. 12 Time fluctuation of AE responses of QSS001: (a) cumulative signal number of each cluster and (b) principal component distribution corresponding to time

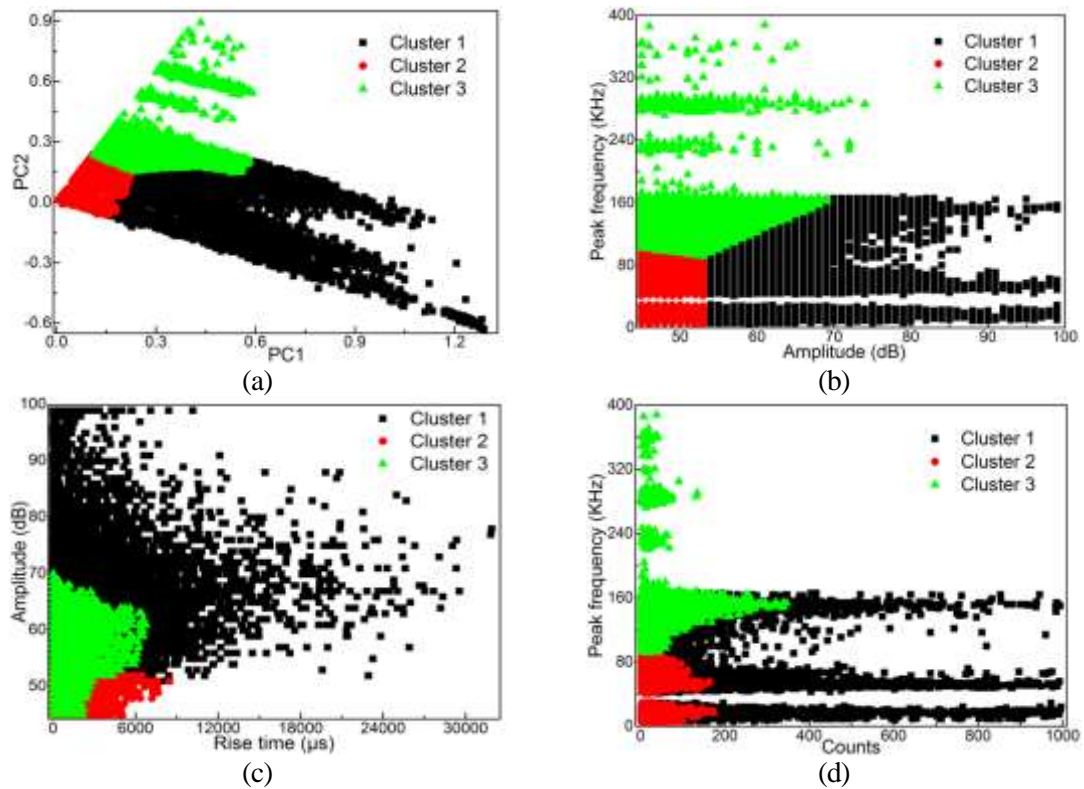


Fig. 13 Correlativity chart of AE features after clustering of QSS001: (a) PC1 vs PC2 distribution; (b) amplitude vs peak frequency distribution; (c) rise time vs amplitude distribution and (d) counts vs peak frequency distribution

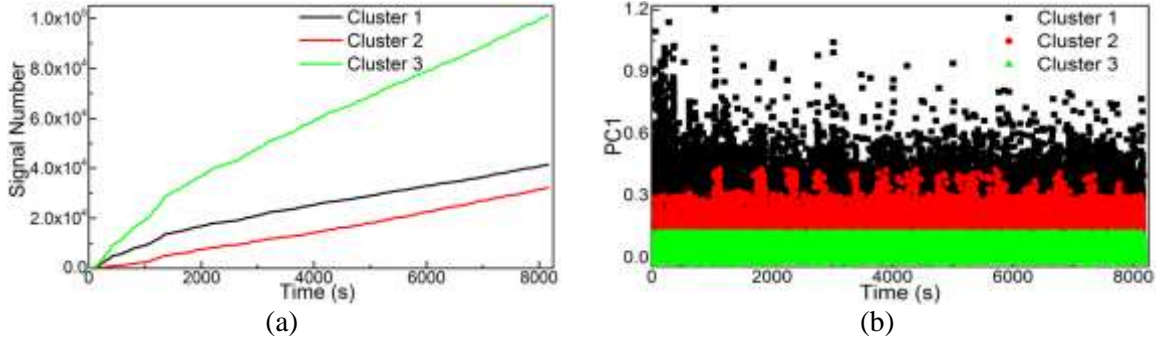


Fig. 14 Time fluctuation of AE responses of QSS301: (a) cumulative signal number of each cluster and (b) principal component distribution corresponding to time

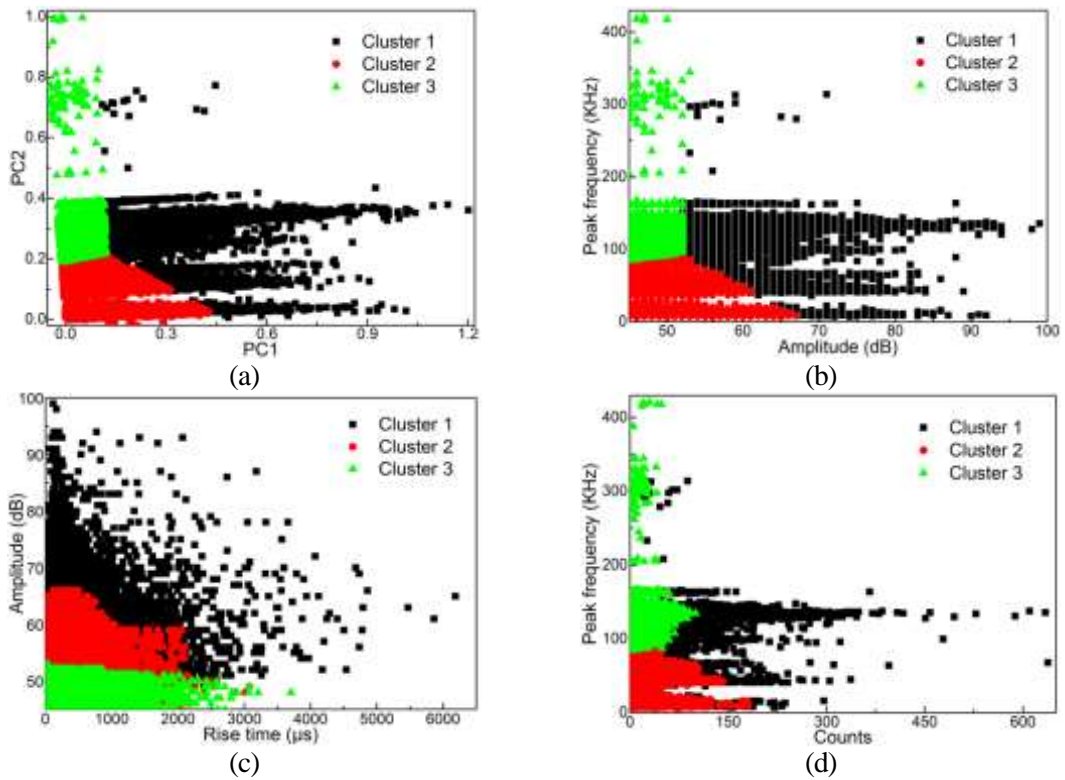


Fig. 15 Correlativity chart of AE features after clustering of QSS301: (a) PC1 vs PC2 distribution; (b) amplitude vs peak frequency distribution; (c) rise time vs amplitude distribution and (d) counts vs peak frequency distribution

Table 7 Statistical analysis of AE features for specimen QSS001

Average AE feature	Rise time ( $\mu$ s)	Counts	Energy	Amplitude (dB)	Peak frequency (kHz)
Cluster 1	925.35	80.54	134.06	60.44	50.61
Cluster 2	248.85	18.33	8.44	48.09	42.53
Cluster 3	186.29	23.24	5.43	51.13	139.62
Total average	398.16	33.07	36.19	51.72	69.87

Table 8 Statistical analysis of AE features for specimen QSS301

Average AE feature	Rise time ( $\mu$ s)	Counts	Energy	Amplitude (dB)	Peak frequency (kHz)
Cluster 1	209.35	62.16	23.03	57.28	128.24
Cluster 2	229.33	23.10	10.55	49.31	40.60
Cluster 3	104.06	16.52	2.80	47.48	132.63
Total average	150.17	28.90	9.01	50.13	114.67

Zitto *et al.* (2015) and Ji *et al.* (2011) concluded that the damage frequency of concrete is primarily concentrated between 20 and 80 kHz. Lai *et al.* (2014) reported that the shear fracture and crushing of concrete are always accompanied by high AE intensity and energy dissipation. Prem *et al.* (2016) and Aggelis *et al.* (2011) proved that AE frequency always decreases during critical shear failure. Zhang *et al.* (2013) conducted AE detection of Q345 steel during a tensile test, and found that the peak frequency of steel damages mainly ranges between 100 and 200 kHz with the amplitude of 50–70 dB during plastic deformation. Saeidi *et al.* (2014) investigated the damage process and mechanisms of dual phase steel and showed that void nucleation is a continuous process that occurs until the final fracture of the material. Kadkhodapour (2011) provided a thorough discussion on void formation, growth, and coalescence for a commercial steel material.

Fig. 12 provides the cumulative signal numbers of each cluster and PC1 distribution corresponding to time for unconfined RC columns. Cluster 2 was continuously distributed throughout the entire damage process with a frequency of 42.53 kHz. Moreover, all AE features, such as amplitude, rise time, and counts, showed low values (Table 7). Thus, Cluster 2 was primarily caused by the generating and closing of concrete micro cracks, and the friction between the faces of cracks and aggregates also result signals in Cluster 2. Clusters 1 and 3 mainly appear after yielding (Fig. 11(a)), and the corresponding signal numbers were only half that of Cluster 2.

Cluster 1 showed high AE feature (rise time, counts, amplitude and energy) values, and its average peak frequency was fixed at 50.61 kHz based on the statistical value of the AE features. Cluster 3 revealed relatively lower AE feature values and a higher peak frequency of 149.62 kHz.

Thus, Cluster 1 was caused by major concrete damages, such as macro interpenetration of existing cracks and crushing of surface concrete. As illustrated in Fig. 7(a), the concrete was crushed and peeled. Cluster 3 could be associated with the yielding damages of steel rebar, including dislocation motion and slipping of steel crystals/grains, which causes irreversible plastic deformation. The exposed and buckled steel rebar is also shown in Fig. 7(a).

With regard to the steel-confined RC columns, Fig. 14 provides the cumulative signal number of each cluster and PC1 distribution corresponding to time. Other steel damages were detected during the damage process. Clusters 1 and 3 have high peak frequencies of 128.24 kHz and 132.63 kHz, respectively, which should be related to steel damage. Cluster 3 was sustained during the entire loading process with relatively low AE features (Table 8) and a large number of damage signals (Fig. 14(a)). According to the fracture mechanism and void development of steel (Kadkhodapour *et al.* 2011), high amplitude signals could be attributed to void coalescence and dislocation motion, whereas low amplitude ones are due to void nucleation and stable growth. Therefore, Cluster 1 mainly contains plastic damages caused by steel crystal dislocation motion, void unstable growth, and coalescence. Fig. 7(b) showed the steel tube yield. Cluster 3 represents void nucleation damages, which occur because of particle fractures and decohesion in the steel tube and rebar. From a micromechanical perspective, the inherent inhomogeneity of grains in steel cause initial defects, which are then activated by external stress and develop into macro damage. Cluster 2 has a low peak frequency (40.60 kHz) and an AE feature value similar to that of the unconfined RC columns. Thus, Cluster 2 represents the formation and closure of micro cracks and friction between faces of cracks and aggregates.

The damage types and mechanisms of the steel-confined and unconfined RC columns under seismic loading were evidently different. AE features, such as peak frequency and amplitude, play a major role in the pattern identification process. For unconfined columns, no steel void nucleation damages were identified because most AE signals were attenuated during propagation in concrete. However, more concrete damage was identified because the concrete was severely damaged, especially around the plastic hinge region (Fig. 7(a)). For the steel-confined columns, more steel damage was determined because the steel tubes were stressed into plastic deformation and AE sensors were fixed directly on the surface of the steel tube. No concrete crushing signals were separated. This finding is supported by the lack of concrete crushing and no macro cracks observed during the test (surface concrete in Fig. 7(b) was removed artificially).

## 6 Conclusions

In this study, the entire damage process of steel-confined and unconfined RC columns under seismic loading was monitored using the AE technique. Quantitative evaluation and pattern recognition were realized on the basis of the recorded AE responses. The major conclusions are as follows:

Energy-based indicators, including ID and relax ratio, successfully disclosed the damage evolution and quantitatively evaluated the damage severity of the columns. A relax ratio of 0.4 indicates initial yielding, whereas an ID of 4.0 and relax ratio of 1.0 mutually support quantitative warnings of the occurrence of severe damage.

The recognized failure patterns and damage types of steel-confined RC columns and unconfined RC columns were different. The FCM algorithm efficiently discriminated the AE data of different generation mechanisms, while statistical analysis of typical AE parameters facilitated

pattern recognition and mechanism illustration from the micromechanical perspective.

The proposed combination of PCA, validity analysis, and FCM cluster incorporates statistical analysis of typical features presents a reliable methodology for structural damage recognition and evaluation. However, the results are based on limited experimental data and theoretical analysis. Thus, further study is needed to enable the in situ application of the presented technique.

## Acknowledgements

The authors are grateful for the financial support from the National Key Research and Development Program of China (Project No. 2017YFC0703410), and National Natural Science Foundation of China (NSFC) under Grant Nos. 51778104.

## References

- Abouhussien, A.A. and Hassan, A.A.A. (2017), "Acoustic emission-based analysis of bond behavior of corroded reinforcement in existing concrete structures", *Struct. Control Health Monit.*, **24**(3), e1893.
- Aggelis, D.G., Soulioti, D.V., Sapouridis, N., Barkoula, N.M., Paipetis, A.S. and Matikas, T.E. (2011), "Acoustic emission characterization of the fracture process in fibre reinforced concrete", *Constr. Build. Mater.*, **25**(11), 4126-4131.
- Behnia, A., Chai, H.K. and Shiotani, T. (2014), "Advanced structural health monitoring of concrete structures with the aid of acoustic emission", *Constr. Build. Mater.*, **65**(65), 282-302.
- Behnia, A., Chai, H.K., Ranjbar, N. and Jumaat, M.Z. (2016), "Damage detection of SFRC concrete beams subjected to pure torsion by integrating acoustic emission and Weibull damage function", *Struct. Control Health Monit.*, **23**(1), 51-68.
- Benavent-Climent, A., Gallego, A. and Vico, J.M. (2012), "An acoustic emission energy index for damage evaluation of reinforced concrete slabs under seismic loads", *Struct. Health Monit.*, **11**(1), 69-81.
- Carpinteri, A., Lacidogna, G. and Niccolini, G. (2011), "Damage analysis of reinforced concrete buildings by the acoustic emission technique", *Struct. Health Monit.*, **18**(6), 660-673.
- Colombo, S., Forde, M.C., Main, I.G. and Shigeishi, M. (2005a), "Predicting the ultimate bending capacity of concrete beams from the "relaxation ratio" analysis of AE signals", *Constr. Build. Mater.*, **19**(10), 746-754.
- Colombo, S., Forde, M.C., Main, I.G., Halliday, J. and Shigeishi, M. (2005b), "AE energy analysis on concrete bridge beams", *Mater. Struct.*, **38**(9), 851-856.
- Davies, D.L. and Bouldin, D.W. (1979), "Cluster separation measure", *IEEE T. Pattern Anal.*, **1**(2), 224-227.
- Droubi, M.G., Faisal, N.H., Orr, F., Steel, J.A. and El-Shaib, M. (2017), "Acoustic emission method for defect detection and identification in carbon steel welded joint", *J. Constr. Steel Res.*, **134**, 28-37.
- Du, F., Li, D., Shan, B. and Wang, Y. (2018), "Failure behavior monitoring and evaluation of steel-confined reinforced concrete columns by acoustic emission under quasi-static loading", *Lat. Am. J. Solids Struct.*, **15**(11), e132.
- Griffin, J. and Chen, X. (2014), "Real-time fuzzy-clustering and CART rules classification of the characteristics of emitted acoustic emission during horizontal single-grit scratch tests", *Int. J. Adv. Manuf. Tech.*, **74**(1-4), 481-502.
- Han, L.H., Liao, F.Y., Tao, Z. and Hong, Z. (2009), "Performance of concrete filled steel tube reinforced concrete columns subjected to cyclic bending", *J. Constr. Steel Res.*, **65**(8), 1607-1616.
- Hongguang, J.I. (2011), "Experimental studies on the frequency characteristics of acoustic emissions in concrete material and its dependences on strength parameters", *Appl. Acoust.*, **30**(2), 112-117.

- Kadkhodapour, J., Butz, A. and Rad, S.Z. (2011), "Mechanisms of void formation during tensile testing in a commercial, dual-phase steel", *Acta Mater.*, **59**(7), 2575-2588.
- Lai, Y.S., Xiong, Y. and Cheng, L.F. (2014), "Frequency band energy characteristics of acoustic emission signals In damage process of concrete under uniaxial compression", *J. Vib. Shock*, **32**(2), 12-19.
- Li, D., Du, F. and Ou, J. (2017), "Damage evaluation of fiber reinforced plastic-confined circular concrete-filled steel tubular columns under cyclic loading using the acoustic emission technique", *Smart Mater. Struct.*, **26**(3), 035014.
- Liu, J., Zhang, S., Zhang, X. and Guo, L. (2009), "Behavior and strength of circular tube confined reinforced-concrete (CTRC) columns", *J. Constr. Steel Res.*, **65**(7), 1447-1458.
- Ma, G. and Li, H. (2017), "Acoustic emission monitoring and damage assessment of FRP-strengthened reinforced concrete columns under cyclic loading", *Constr. Build. Mater.*, **144**, 86-98.
- Manson, G., Worden, K., Holford, K. and Pullin, R. (2001), "Visualisation and dimension reduction of acoustic emission data for damage detection", *J. Intel. Mat. Syst. Str.*, **12**(8), 529-536.
- Marec, A., Thomas, J.H. and El Guerjouma, R. (2008), "Damage characterization of polymer-based composite materials: Multivariable analysis and wavelet transform for clustering acoustic emission data", *Mech. Syst. Signal Pr. Special Issue: Mechatronics*, **22**(6), 1441-1464.
- Pashmforoush, F., Fotouhi, M. and Ahmadi, M. (2012), "Damage characterization of glass/epoxy composite under three-point bending test using acoustic emission technique", *J. Mater. Eng. Perform.*, **21**(7), 1380-1390.
- Prem, P.R. and Murthy, A.R. (2016), "Acoustic emission monitoring of reinforced concrete beams subjected to four-point-bending", *Appl. Acoust.*, **117**, 28-38
- Saeidi, N., Ashrafzadeh, F., Niroumand, B., Forouzan, M.R. and Barlat, F. (2014), "Damage mechanism and modeling of void nucleation process in a ferrite-martensite dual phase steel", *Eng. Fract Mech.*, **127**, 97-103.
- Sagar, R.V., Prasad, B.K.R. and Singh, R.K. (2015), "Kaiser effect observation in reinforced concrete structures and its use for damage assessment", *Arch. Civ. Mech. Eng.*, **15**(2), 548-557.
- Sahu, H.B., Mahapatra, S.S. and Panigrahi, D.C. (2012), "Fuzzy C-means clustering approach for classification of Indian coal seams with respect to their spontaneous combustion susceptibility", *Fuel Process Technol.*, **104**, 115-120.
- Wang, Y., Wang, W., Zhou, X. and Liu, J. (2017), "Experimental study on seismic behavior of steel tube confined reinforced concrete columns subjected to combined compression-bending-torsion", *J. Build. Struct.*, **38**(1), 185-189.
- Xie, X.L. and Beni, G. (1991), "A validity measure for fuzzy clustering", *IEEE T. Pattern Anal.*, **13**(13), 841-847.
- Zhang, Y., Zhao, G., Zhou, J. and Zhu, R. (2013), "Acoustic emission analysis of frequency characteristic for 20 # steel during tensile process", *Chem. Machinery*, **40**(5), 569-573.
- Zhou, X., Zhang, S. and Liu, J. (2008), "Seismic behavior of steel tube confined reinforced concrete (RC) beam-columns", *J. Build. Struct.*, **29**(5), 75-84.
- Zitto, M.E., Piotrkowski, R., Gallego, A., Sagasta, F. and Benavent-Climent, A. (2015), "Damage assessed by wavelet scale bands and b-value in dynamical tests of a reinforced concrete slab monitored with acoustic emission", *Mech. Syst. Signal Pr.*, **60-61**, 75-89.